Optics & Laser Technology 161 (2023) 109179

Contents lists available at ScienceDirect

Optics and Laser Technology

journal homepage: www.elsevier.com/locate/optlastec

Full length article

Weld-penetration-depth estimation using deep learning models and multisensor signals in Al/Cu laser overlap welding

Sanghoon Kang [a,b], Kidong Lee [c], Minjung Kang [a], Yong Hoon Jang [b,*], Cheolhee Kim [a,c,*]

[a] Joining R&D Group, Korea Institute of Industrial Technology, Incheon, Republic of Korea
[b] School of Mechanical Engineering, Yonsei University, Seoul, Republic of Korea
[c] Department of Mechanical and Materials Engineering, Portland State University, Portland, USA

ARTICLE INFO

Keywords:
Laser welding
Al/Cu overlap joint
Penetration-depth estimation
Image sensor
Photodiode
Deep learning

ABSTRACT

Al/Cu laser-welded overlap joints, in which weld-penetration depth significantly influences both joint strength and electrical conductivity, are widely applied in automotive battery cells. In this study, a unisensor convolutional neural network (CNN) model that predicts penetration depth using coaxial weld-pool images as input and multisensor CNN models that utilize additional photodiode signals are proposed. The penetration depth was estimated using an optical coherence tomography sensor. The coefficient of determination values for the unisensor and multisensor CNN models were between 0.982 and 0.985, and their mean absolute errors were between 0.0278 and 0.0302 mm. The short-term Fourier transform multisensor model presented the best performance in terms of prediction of penetration depth when applied to the photodiode signal. The proposed prediction models were validated using a gradually varying laser power experiment, which demonstrated the efficacy of this approach and its potential use in automotive applications. Keywords: Laser welding, Al/Cu overlap joint, Penetration-depth estimation, Image sensor, Photodiode, CNN, Deep learning.

1. Introduction

In keyhole-mode laser welding, a thin capillary referred to as a laser keyhole is irradiated with a laser beam that is reflected multiple times within the keyhole. During multiple reflections of the laser beam, energy is transferred from the laser beam to the weld-pool surface by Fresnel absorption. The main heat-transfer mechanism for keyhole-mode laser welding involves multiple reflections, which enables a high aspect ratio—the ratio of penetration depth to bead width—within the cross-section of the weld. The weld width provides a good estimate of the weld-penetration depth in conventional arc welding and conduction-mode laser welding, excluding the disturbances caused by the Marangoni effect. However, the penetration depth in keyhole-mode laser welding is independent of bead width, owing to the multiple reflections within the laser keyhole. Modeling the penetration depth while considering multiple reflections is inherently complex. It is also practically impossible to predict penetration depth based on process variables; however, several analytical models have been proposed for this purpose [1-4].

Copper and aluminum alloys are the main materials used for the electric interconnections of lithium-ion battery cells, and the dissimilar-metal joining between these alloys is indispensable in battery manufacturing [5]. However, even when the joining does not involve dissimilar metals, copper and aluminum alloys have poor weldability owing to their high thermal and electrical conductivity, and high laser reflectivity. Welding Cu/Al dissimilar-metal combinations is further complicated by differences in melting temperatures and intermetallic compounds. Sufficient electrical conductance and joint strength are necessary for the welded Al/Cu joints of battery cells. Therefore, laser welding is preferred because it has higher joint strength and electrical conductance per contact area than those provided by resistance spot welding and ultrasonic welding [6,7].

To ensure adequate connection characteristics, laser-welded overlap joints require a large bead width at the faying surface and an adequate weld penetration. The bead width at the faying surface is hereafter referred to as the interface bead width. A large interface bead width increases the available area for electric current flow and mechanical load bearing. However, an excessive bead width is accompanied by a high heat input into the weldment, which results in thermal distortion, strength degradation, and detrimental intermetallic compound growth.

* Corresponding authors at: School of Mechanical Engineering, Yonsei University, Seoul, Republic of Korea (Y.H. Jang). Joining R&D Group, Korea Institute of Industrial Technology, Incheon, Republic of Korea (C. Kim).
E-mail addresses: jyh@yonsei.ac.kr (Y.H. Jang), chkim@kitech.re.kr, cheol@pdx.edu (C. Kim).

https://doi.org/10.1016/j.optlastec.2023.109179
Received 10 June 2022; Received in revised form 26 August 2022; Accepted 10 January 2023

In a study by Solchenbach et al. [8], a homogeneous interface between Al and Cu was formed in a "good-weld" case, compared with the "cold-weld" and "over-weld" cases. In the "cold-weld" case, insufficient heat input caused incomplete diffusive bonding between Al and Cu, and in the "over-weld" case, excessive heat input into the lower part of the overlap joint caused abundant dilution that resulted in cavities and pores within the melting zone.

Monitoring penetration characteristics, such as interface bead width and penetration depth, during laser welding is not straightforward. The shapes of the weld pool and solidified weld bead may be easily observed from the top surface of the weldment using image sensors. However, the appearance of the weld pool and bead cannot be used as a direct measure of the penetration characteristics in keyhole-mode laser welding because the weld pool and bead have a wide range of aspect ratios.

Laser-welding phenomena are intrinsically nonlinear, and neural network models have been developed to evaluate laser welding quality [9,10]. Lee et al. developed a neural network model to estimate weld-pool penetration from top-view weld-pool images that were acquired during pulsed laser welding; however, this application was limited to conduction-mode welding [11,12]. Zhang et al. [13] proposed a multi-sensor model to monitor laser-welding quality using multiple optical sensors and estimated the formation of weld defects, such as blow out, humping, and undercuts. Zhang et al. [14] proposed a deep learning model to monitor the porosity formation in weld beads using coaxial high-speed images of the weld pool. Zhang et al. [15] constructed a penetration-mode classification neural network model based on coaxial high-speed imaging. Lee et al. [16], Go et al. [17], and You et al. [18] demonstrated that using neural network models, penetration depth and interface bead width can be estimated from material combination and process parameters; however, these studies were not extended to *in situ* monitoring and prediction. More recently, the authors of this study evaluated the performance of various machine learning models in estimating the laser-weld penetration of Al/Cu overlap joints using photodiode signals [19]. A band-pass filter was employed on the photodiode to detect a specific wavelength of Cu emission, and the penetration mode was successfully predicted.

To the best of the authors' knowledge, *in situ* penetration depth prediction of keyhole-mode laser welding using neural network models has not been previously reported.. Therefore, in the present study, deep learning models were employed to model a high-order nonlinear relationship between weld-pool creation and penetration depth in the lower sheet of the overlap joint. Coaxial weld-pool images and photodiode signals were used as inputs for the deep learning models. To evaluate model performance, tests were performed using a unisensor signal from an image sensor and multisensor signals from an image sensor and a photodiode.

2. Data preparation

2.1. Experiments

The base materials included an Al 1050 alloy and a Cu C1100 alloy with a thickness of 0.4 and 1.0 mm, respectively. The chemical compositions and mechanical properties of the base materials are listed in Tables 1 and 2, respectively. The specimens were machined to a length of 150 mm and width of 50 mm. An Al sheet was placed on a Cu sheet in a completely overlapping configuration, and the weld length was 100 mm along the longitudinal direction at the center of the specimen.

Table 2
Mechanical properties of base materials.

	Tensile strength (MPa)	Elongation (%)
Al 1050	15.8	5
C1100	268	27.5

The experimental setup is shown in Fig. 1. A laser beam with a power of 3 kW and a wavelength of 1,030 nm was generated using a continuous-mode Yb:YAG laser generator (Trudisk 3002, Trumpf GmbH, Germany). The beam was delivered through an optical fiber with a diameter of 0.2 mm and optics with a focal length of 300 mm. The laser beam was focused on the top surface of the specimen, and the beam diameter at the focal position was 0.3 mm.

A high-speed camera (Mini UX30, FASTCAM, Japan) and photodiode were employed as input sensors. The high-speed camera was connected to the dichroic mirror in the optics, and coaxial images were collected at a frame rate of 10,000 fps and an exposure time of 1/10,000 s. The images had a resolution of 768 pixels in width and 232 pixels in height. To minimize the effect of laser-induced plasma and plumes on image acquisition, the specimen surface was illuminated with a 120 W diode laser beam of 808 nm wavelength. A band-pass filter and a neutral density (ND) filter were installed in front of the camera lens; the band-pass filter had a center wavelength of 808 nm, a full width at half maximum (FWHM) of 1.5 nm, and an ND8 filter.

A photodiode that is sensitive in the wavelength range of 200–1,100 nm was installed at an inclination of 45° with respect to the welding direction, and it was aimed towards the laser focal point. The distance between the end of the photodiode and laser focal point was 85 mm. A band-pass filter with a center wavelength of 580 nm and a FWHM of 5 nm was applied to detect a specific Cu emission [19]. Voltage signals from the photodiode were sampled at a frequency of 50 kHz using an analog-to-digital converter (NI 9234, National Instruments, USA).

The output of the deep learning model was set as the penetration depth. Penetration measurement through cross-sectioning presents a limitation in terms of the number of data points that can be collected. A keyhole-depth monitoring device (WDM, Trumpf GmbH, Germany) was used for real-time and high-frequency penetration-depth estimation. The WDM was used to measure keyhole depth using optical coherence tomography (OCT). The measurement range and sampling frequency were set to values up to 8.0 mm and 7 kHz, respectively. Using the keyhole-depth measurement from the WDM, this study calibrated the relationship between keyhole depth and penetration depth that was determined in a previous study that employed the same material combination and welding parameters [19].

Welding experiments were conducted under twenty-five different welding conditions. The welding speed was varied from 3 to 7 m/min, in 1 m/min increments. Five laser powers per welding speed were selected to implement various penetration modes, ranging from partial melting of the upper Al plate to stable penetration into the lower Cu plate. Throughout the entire experiment, the laser power ranged from 1.1 to 1.6 kW.

Continuous OCT output signals, photodiode signals, and coaxial images were recorded in sync. Only the middle signals, excluding 0.3 s at both the welding start and end, were used for modeling.

After modeling, a verification welding run was conducted. In the

Table 1
Chemical composition of base materials (wt%).

Al 1050	Al	Si	Fe	Cu	Mn	Mg	Zn	Ti	V
	99.59	0.068	0.286	0.003	0.001	0.001	0.002	0.023	0.016
C1100	Cu								
	99.959								

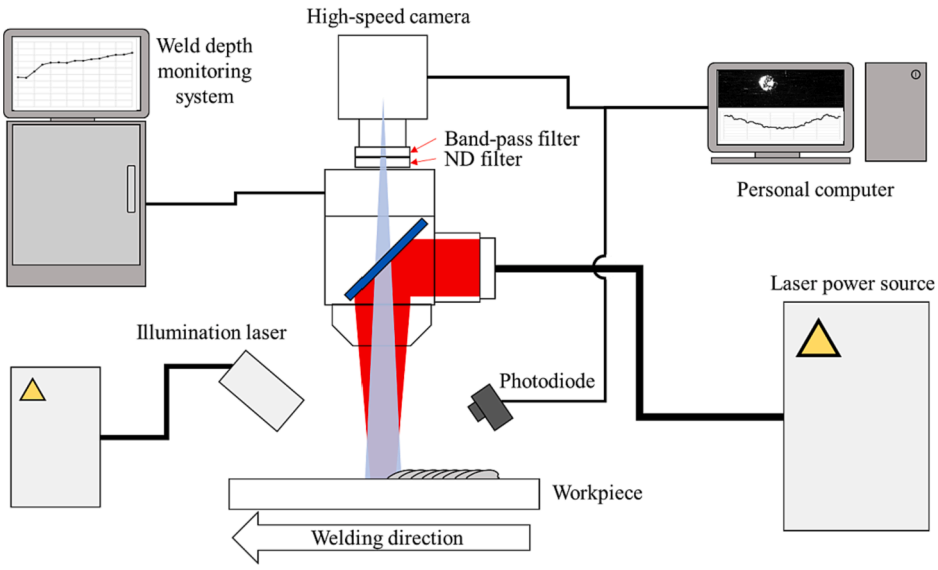

Fig. 1. Schematic diagram of the proposed data acquisition system.

verification run, the laser output power was increased from 1,100 to 1,500 W, and the welding speed was fixed at 3 m/min. The welded specimen was cut along the longitudinal centerline, and the penetration depth profile measured using optical microscopy was compared with the penetration depth estimated using the proposed deep learning models.

2.2. Data preprocessing

In the proposed system, the high-speed camera was used as the primary sensor, and the photodiode as an auxiliary sensor. Four models were developed for the real-time estimation of weld penetration—one unisensor model using weld-pool images as input, and three multisensor models using photodiode signals and weld-pool images as input. In the multisensor models, the photodiode signals were preprocessed according to the following signal processing methods: (1) downsampling in the time domain, (2) fast Fourier transform (FFT), and (3) short-term Fourier transform (STFT). For all models, the output was the penetration depth measured using the OCT device. The original frequencies of imaging, photodiode A/D conversion, and OCT sampling were 10, 50, and 7 kHz, respectively, and these were resampled at 0.1 kHz by averaging the raw signals, as described below.

a. Image preprocessing

Images recorded at a frequency of 10 kHz were downsampled to 0.1 kHz by averaging the intensity per pixel for every 100 images, as shown in Fig. 2. Here, m, n, l, I, and I^s denote the vertical resolution (232), horizontal resolution (768), number of averaged images (100), intensity at the pixel, and averaged intensity at the pixel, respectively. The subscripts i, j, and k indicate the pixel location. The averaging algorithm provided a software low-pass-filtering effect, thus reducing noise (Fig. 3). Although the edge lines were slightly blurred, the keyhole and edge features were highlighted after preprocessing.

b. Time-series signal preprocessing

In the time-domain multisensor model, photodiode and OCT signals were downsampled to 0.1 kHz. This approach of downsampling by averaging was applied to the time-series signals, as shown in Fig. 4. Here, n, l, V, and V^s denote the number of signals per unit raw data sample, length of averaging, raw signal sample, and averaged signal sample, respectively. The subscripts i and j indicate the signal location.

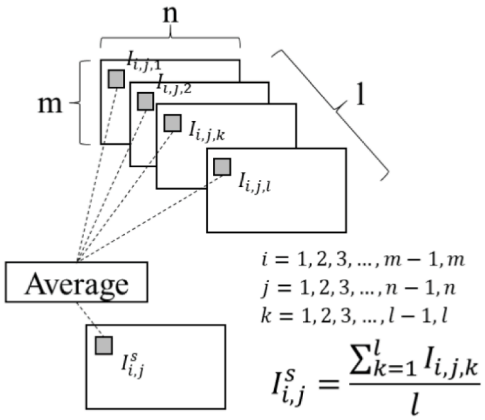

Fig. 2. Downsampling of images using the proposed sampling approach and averaging algorithm.

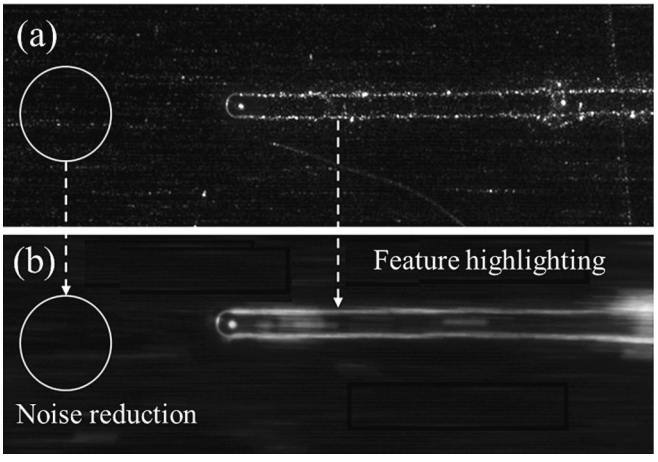

Fig. 3. Comparison of (a) original image and (b) preprocessed image using the proposed algorithm.

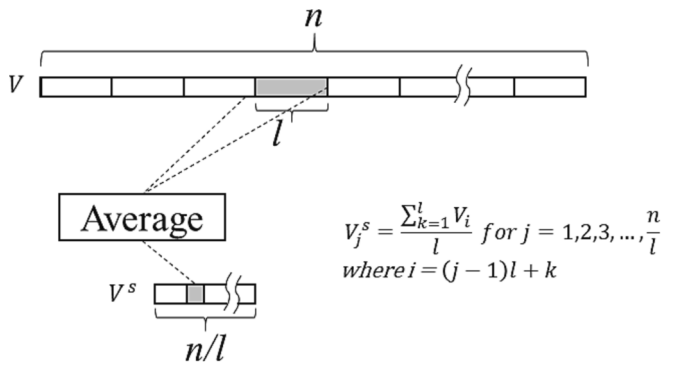

Fig. 4. Downsampling of time-series data using the proposed averaging method.

The lengths of averaging for the photodiode and OCT signals were 5 and 70, respectively. Thus, the sampling rates after preprocessing were 10 kHz for the photodiode signal and 0.1 kHz for the OCT signal. Consequently, one data point for the time-domain multisensor model consisted of an input 232 × 768 pixels image and 100 photodiode signals, and an output of one OCT signal.

In the FFT and STFT multisensor models, data points were prepared at a sampling rate of 0.1 kHz. The downsampling approaches for both image and OCT signals were as described above. In the FFT model, a spectrum of 500 frequency-domain characteristics were derived from 500 photodiode signals. One data point of the FFT model consisted of a 232 × 768 pixels image and a spectrum with 500 frequency-domain characteristics for the photodiode signal as input, and one OCT signal as output. In the STFT model, the 500 photodiode signals were transformed into an STFT spectrogram, a time–frequency characteristics matrix with a dimension of 23 (time) × 23 (frequency). One data point of the STFT model included a 232 × 768 pixels image and 23 × 23 STFT spectrogram as input, and one OCT signal as output.

Fig. 5a shows the raw and preprocessed photodiode signals. Despite signal smoothing due to averaging, the averaged signal sufficiently represented the raw signal characteristics. Fig. 5b and c show examples of the photodiode signal frequency-domain characteristics. Although the frequency-domain characteristics presented relatively low resolution, they were used in the modeling without further adjustment to maintain the response speed. Fig. 6 shows the raw and preprocessed OCT signal. The averaged OCT signal exhibited a slight time delay with respect to the raw signal because the sampling rate of the downsampled OCT signal was relatively slow.

2.3. Deep learning models

Unisensor and multisensor models were investigated in this study, as shown in Fig. 7. The unisensor model was a typical convolutional neural network (CNN) model with an input comprised of CCD images. In the unisensor model, a CNN with two convolution, batch normalization, and max pooling layers was connected to a fully connected neural network (FCN) with two dense layers (Fig. 7a). A rectified linear unit (ReLU) function was chosen as the activation function at all nodes, with the exception of the output layer nodes, where an identical function was applied as the activation function. In the multisensor models, one of three networks used for the photodiode signal was concatenated with a two-dimensional CNN model of the image before the FCN layers (Fig. 7b). The time-domain model was composed using a one-dimensional CNN for the photodiode signal. One-dimensional CNN models are known to be good substitutes for recurrent neural networks (RNNs) in modeling time-series signals because of reduced calculation costs [20]. Moreover, a one-dimensional CNN model showed excellent penetration-mode prediction performance in a previous study [19]. Additionally, the structure of the CNN model was similar to that of the

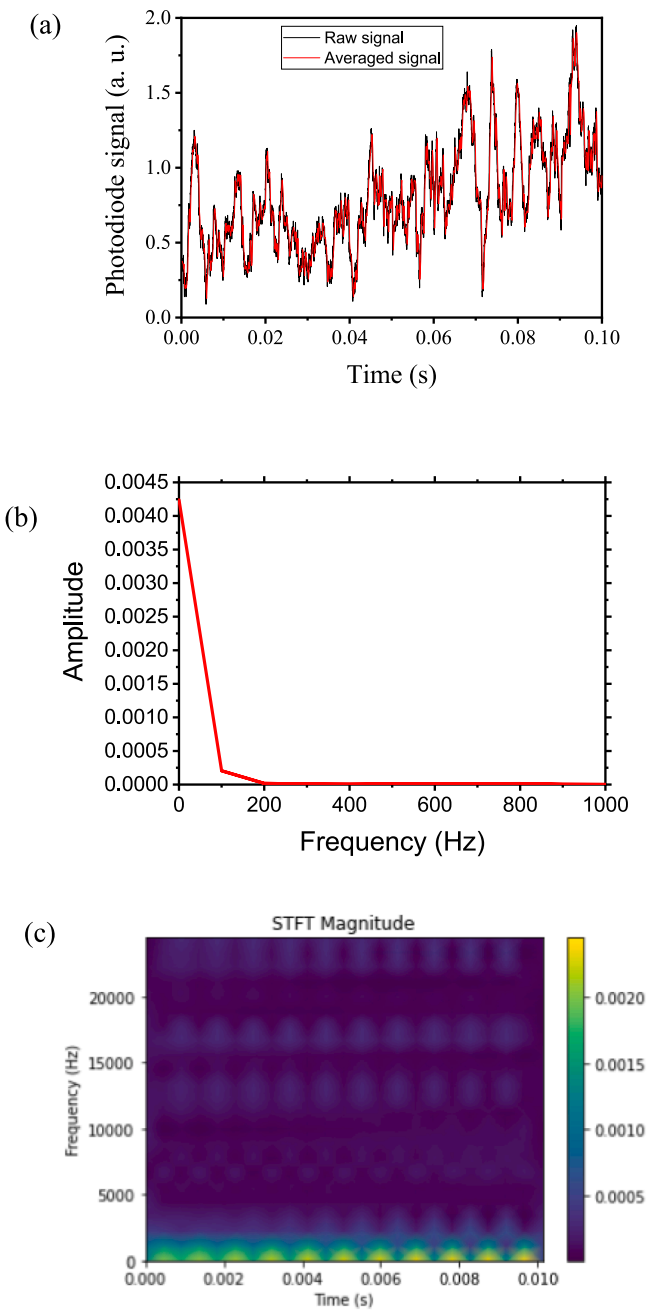

Fig. 5. Photodiode signal processing (laser power: 1,484 W, welding speed: 7 m/min). (a) Raw and downsampled time-domain signal, (b) FFT spectrum, and (c) STFT spectrogram.

CNN for the CCD image, with the exception of the kernel size in the convolution layers. The STFT model was developed using a 2D CNN for the STFT magnitude. The FFT model used the FFT characteristics directly without the use of a neural network.

2.4. Deep learning model training

2.4.1. Training and validation

After data preprocessing, 2,115 data points were randomly divided into training, validation, and test datasets, which contained 1480, 317, and 318 data points, respectively. The mean square error (MSE) loss function and an Adam optimizer [21] were used for model training. The parameters for the Adam optimizer were as follows: learning rate of 10^{-3}, $\beta_1 = 0.9$, $\beta_2 = 0.999$, and $\varepsilon = 10^{-8}$. The model was trained for 1000

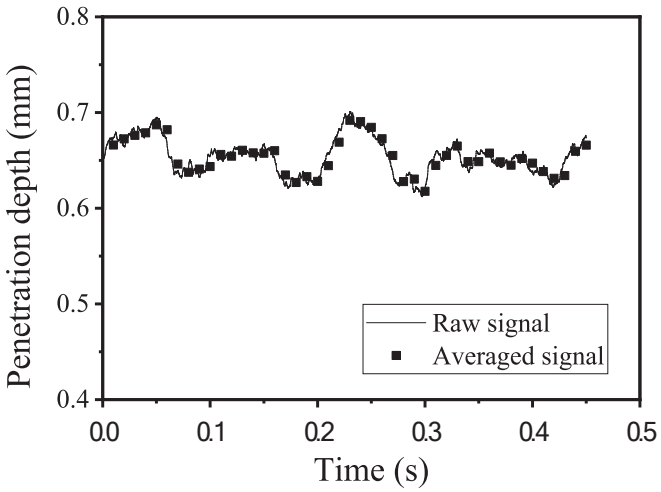

Fig. 6. Measured and downsampled penetration depth using the proposed system (laser power: 1,484 W, welding speed: 7 m/min).

epochs with mini batches of 16 data points.

Neither the unisensor CNN model nor the multisensor models were overfitted during model training (Fig. 8). The loss for the training dataset decreased with the increase in the epoch number over the entire test range, whereas the loss for the validation dataset saturated after the 300th epoch.

The trained CNN models presented a nearly perfect prediction capability (Tables 3 and 4). The coefficients of determination (R^2) for the unisensor model were 0.99986 and 0.98150 for the training and validation datasets, respectively. The mean absolute errors (MAEs) for the training and validation datasets were only 0.00273 and 0.03020 mm, respectively. The MAE for the multisensor CNN models were slightly higher on the training data, but lower on the test data. The STFT multisensor model showed the best performance, both in terms of MAE and R^2.

2.5. Model test

The coefficient of determination and MAE in the model tests were similar to those obtained in the model validation because the trained models were not overfitted (Fig. 9). The MAEs for the unisensor and multisensor models were between 0.02782 and 0.0302 mm, respectively. In the residual plot, the interquartile ranges (IQRs) for the unisensor and multisensor models were between 0.04468 and 0.04816 mm (Fig. 10). These values are approximately 1/10th the thickness of the top plate; thus, they are within an acceptable tolerance range for the estimation of penetration depth during high-power laser welding.

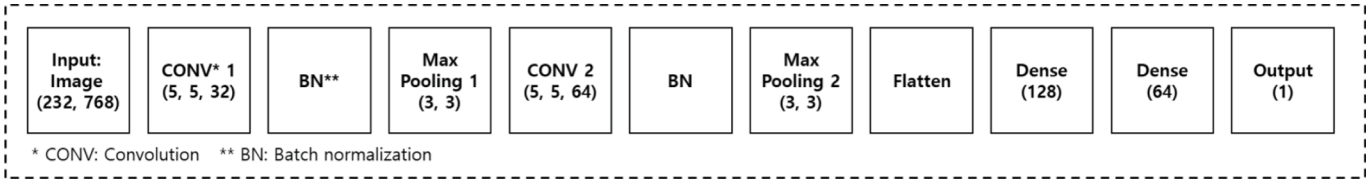

(a)

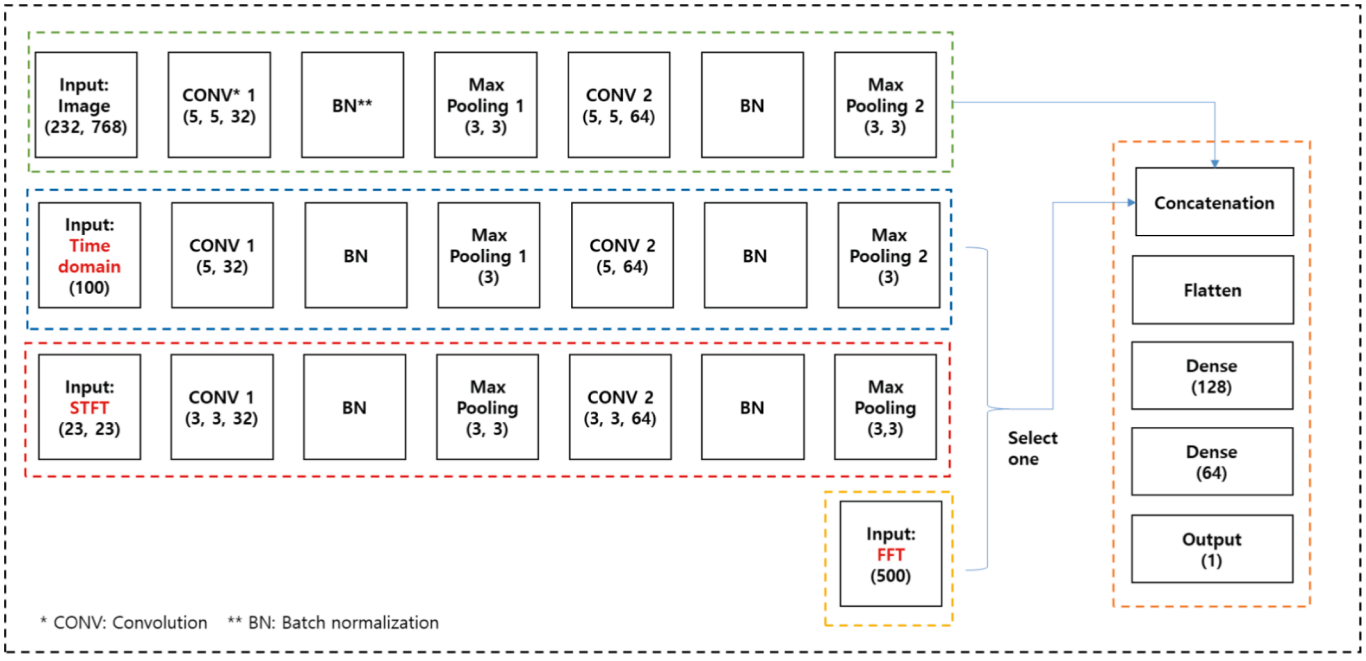

(b)

Fig. 7. Architecture of the developed CNN models. (a) Unisensor model and (b) multisensor model.

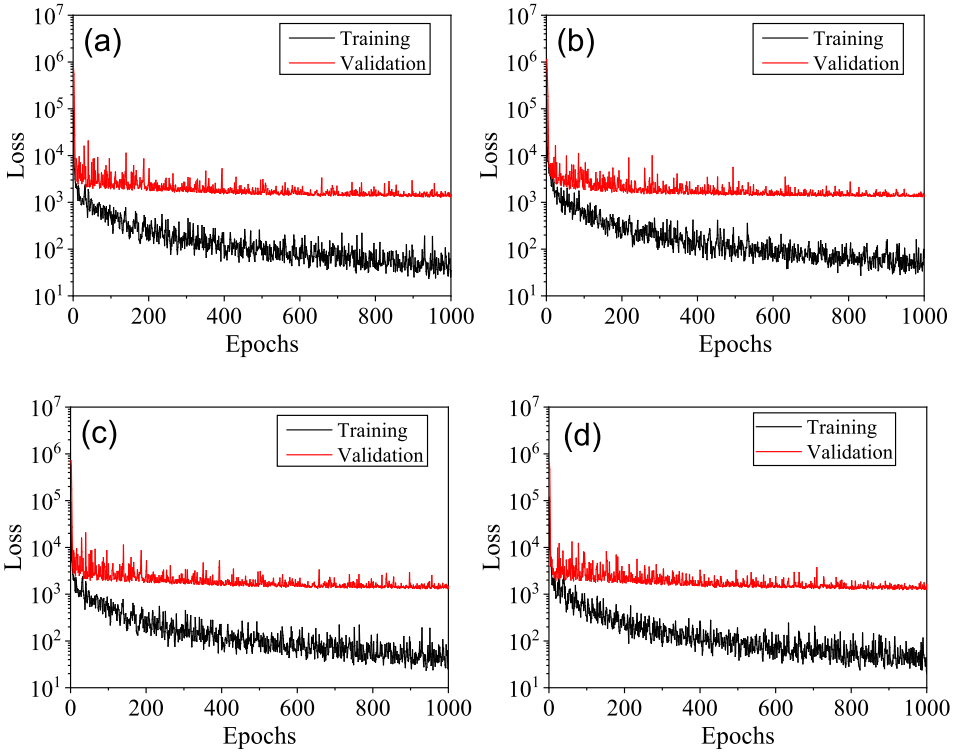

Fig. 8. Training and validation losses for (a) unisensor, (b) time-domain multisensor, (c) STFT multisensor, and (d) FFT multisensor CNN models.

Table 3
Mean absolute error of trained models (mm).

	Unisensor	Time-domain multisensor	STFT multisensor	FFT multisensor
Training data	0.00273	0.00488	0.00330	0.00254
Validation data	0.03155	0.02998	0.02839	0.02821
Test data	0.03020	0.02782	0.02782	0.02814

Table 4
Coefficient of determination, R^2 of trained models.

	Unisensor	Time-domain multisensor	STFT multisensor	FFT multisensor
Training data	0.99986	0.99958	0.99979	0.99990
Validation data	0.98071	0.98260	0.98411	0.98472
Test data	0.98150	0.98430	0.98510	0.98471

2.6. Verification

To verify the trained deep learning models, a welding trial was conducted by gradually increasing the laser power. The laser power was increased from 1,100 to 1,500 W for a welding length of 100 mm, while the welding speed was fixed at 5 m/min. During welding, the sensor signals were acquired, and the penetration depth was predicted using the unisensor and time-domain multisensor models.

After the welding trial, the specimen was cut along the centerline in the longitudinal direction, and the cross-section was imaged by combining multiple images, as shown in Fig. 11. The fusion line profiles between the two arrows in Fig. 11 were extracted using image processing. The measured profiles were compared with the predicted penetration depths (Fig. 12). The MAEs for the unisensor and multisensor models were 0.0343 and 0.0298 mm, respectively, which are approximately 10 % higher than the MAEs in the model test results presented in the previous section, but within an acceptable tolerance level.

3. Discussion

This study is the first deep learning investigation that focusses on real-time and quantitative penetration-depth prediction in partial-penetration mode, rather than focusing on qualitative penetration-mode prediction. In previous studies, deep learning-based models have been used to classify welding quality [13,22-25], penetration mode [15,19,26,27], porosity [14], and spatter detection [28]. The CNN-based deep learning models employed in this study were able to accurately predict real-time penetration depth in Al/Cu dissimilar-metal laser welding. Among the models that were investigated, the STFT multisensor model showed the best accuracy. STFT is a type of feature-extraction algorithm in the frequency-domain that also contains time-localized characteristics. In the STFT multisensory model, a 2D CNN for the image and 2D CNN for the STFT spectrogram were concatenated, in an approach that showed excellent feature extraction and regression performance.

In the coaxial monitoring of the weld pool during laser overlap welding, geometric features for the following physical objects may be characterized from images: (1) the molten pool, (2) keyhole, and (3) penetration hole [29,30]. The penetration hole was only observed when the keyhole fully penetrated the bottom of the overlap joint. Keyhole appearance is not an appropriate feature for determining penetration depth because various aspect ratios are implemented for the same keyhole opening in keyhole-mode laser welding. Additionally, the molten pool shapes are dependent on the heat input for the base metals, which affects the penetration depth. However, pool shapes cannot be used as the sole determinant of penetration depth because they undergo abrupt changes during a shift in penetration mode [29]. In the proposed models, penetration depth could be precisely predicted from a top-view image, which contains information on the keyhole, weld pool, and

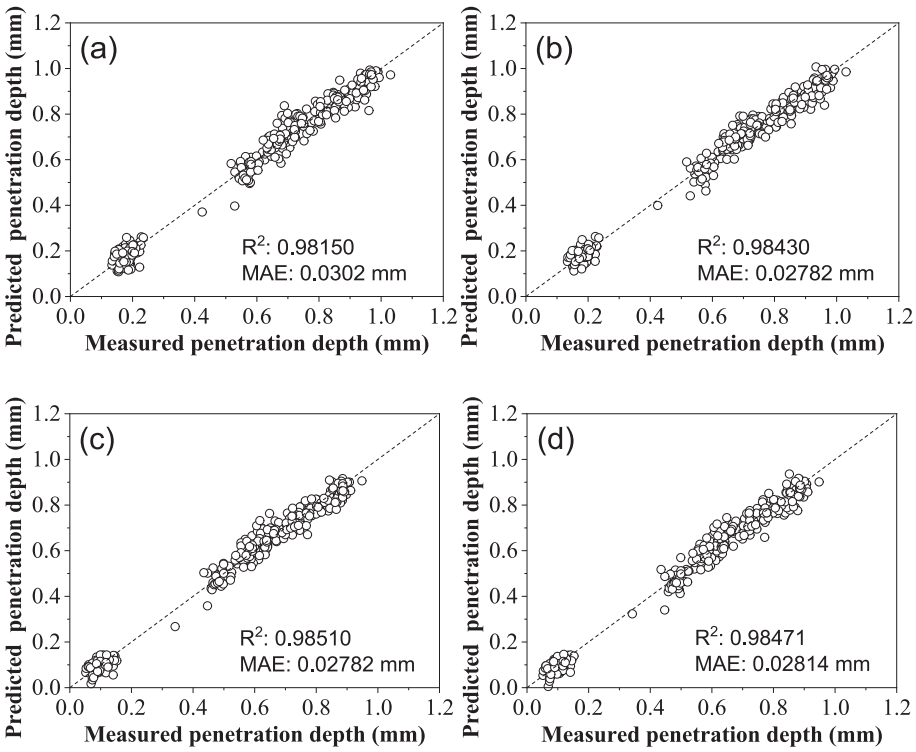

Fig. 9. Model evaluation using test dataset: (a) unisensor, (b) time-domain multisensor, (c) STFT multisensor, and (d) FFT multisensor CNN models.

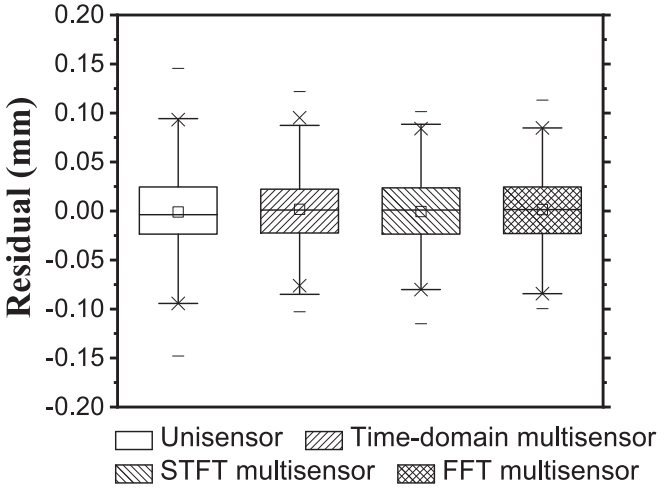

Fig. 10. Residual plot for the test dataset obtained using the proposed approach.

solidified weld bead.

Photodiodes are low-cost and high-sampling-rate devices used to evaluate welding phenomena, and their application to welding quality and stability assessment in laser welding has been well established. In the infrared, visible, and ultraviolet wavebands, photodiodes are able to detect thermal radiation, material emission, laser reflection, and laser-induced plasma [31-35], and they have been successfully transplanted from research to industry. However, photodiodes provide low resolution, and their output is a unitless magnitude used to show relative spectral response, which is sensitive to the measuring location, focus, angle, and distance of sensor, base materials, and process parameters. Thus, photodiode-based sensors require a reference for each application to set classification criteria, and their role has been limited to discrete and qualitative evaluation. The proposed photodiode-sensor system had a wavelength band that was specified according to the base metal employed and was selected as an auxiliary sensor in quantitative evaluation. The photodiode had a sampling rate of 50 kHz that is much higher than the dataset sampling rate of 0.1 kHz. Moreover, 500 photodiode signals per data point may be used to enhance the accuracy of a prediction model. CNNs are famous for their local spatial feature-extraction capability that compensates for the relative nature of photodiode signals.

The collection of a large number of data points is extremely important when building deep learning models. Real-time data acquisition for model inputs and outputs facilitates mass data collection; however, this is limited for welding data, particularly in terms of output data. Welding penetration data are traditionally collected from the transverse cross-section [17,36] and longitudinal cross-section [14,19]. The OCT has been recently introduced to measure laser keyhole depth and estimate penetration depth [37,38]. Although OCT measurement is inherently sensitive to both keyhole stability and measuring laser beam location [39], a number of investigations have been conducted into its

Fig. 11. Evolution of the longitudinal cross-section of the specimen with gradually increasing laser power (welding speed: 3 m/min; weld length: 100 mm; initial laser power: 1,100 W; final laser power: 1,500 W).

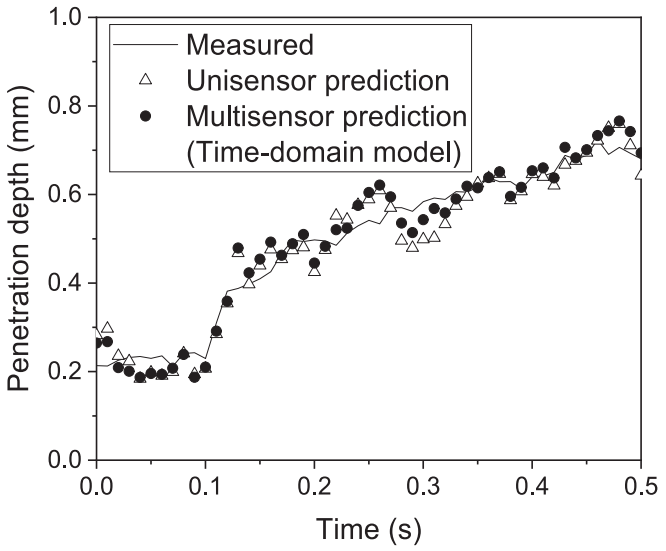

Fig. 12. Measured and predicted weld penetration using the proposed approach, with a gradual increase in laser power.

application to pore detection [38], weld seam tracking [40], weld depth monitoring [39,41], and OCT surface quality classification [42,43]. In this study, the OCT signal was employed as an output sensor to collect numerous data points without the need for time-consuming cross-sectioning. The OCT sensor signal was stabilized using downsampling, and the penetration depth was effectively determined using the relationship between the OCT signal and penetration depth.

4. Conclusions

In this study, the proposed deep learning models were shown to predict *in situ* penetration depth during laser welding of Al/Cu overlap joints. A unisensor model using top-view images and multisensor models utilizing auxiliary photodiode sensor signals were proposed, and the following conclusions were drawn.

- Unisensor and multisensor CNN models were constructed to predict penetration depth. These regression models presented excellent accuracy, providing determination coefficient (R^2) values of 0.02782 and 0.0302, and MAEs of approximately 10 % of upper plate thickness.
- The models were constructed using coaxial weld-pool images and photodiode signals as inputs and the OCT signal as output. Laser illumination and a band-pass filter enhanced the reliability of the input sensors. The OCT signal was successfully used as a real-time penetration depth sensor for the detection of keyhole depth.
- The STFT multisensor model showed the best performance among the models, in terms of penetration-depth prediction. In this model, a 2D CNN for the image and 2D CNN for the STFT spectrogram were concatenated.
- In a verification experiment conducted using a gradually increasing laser power, penetration depth was accurately predicted by both the unisensor and multisensor models, with MAEs of 0.0343 and 0.0298 mm, respectively.

Therefore, the proposed deep learning models were successfully employed in the prediction of real-time penetration depth in partial-penetration mode.

CRediT authorship contribution statement

Sanghoon Kang: Conceptualization, Methodology, Writing – original draft. **Kidong Lee:** Software, Data curation. **Minjung Kang:** Investigation, Project administration, Funding acquisition. **Yong Hoon Jang:** Supervision. **Cheolhee Kim:** Writing – review & editing, Supervision.

Declaration of Competing Interest

The authors declare that they have no known competing financial interests or personal relationships that could have appeared to influence the work reported in this paper.

Data availability

No data was used for the research described in the article.

Acknowledgements

We acknowledge financial and technical support provided by the Korea Institute of Industrial Technology (EH-22-060). We are pleased to acknowledge support from the National Research Foundation of Korea (NRF) funded by the Korea government (MSIP) (Grant No. 2021R1A2C3010731).

References

[1] A. Kaplan, A model of deep penetration laser welding based on calculation of the keyhole profile, J. Phys. D: Appl. Phys. 27 (9) (1994) 1805–1814.
[2] H. Ki, J. Mazumder, P.S. Mohanty, Modeling of laser keyhole welding: Part I. Mathematical modeling, numerical methodology, role of recoil pressure, multiple reflections, and free surface evolution, Met. Mater. Trans. A 33 (6) (2002) 1817–1830.
[3] H. Zhao, T. DebRoy, Macroporosity free aluminum alloy weldments through numerical simulation of keyhole mode laser welding, J. Appl. Phys. 93 (12) (2003) 10089–10096.
[4] J.-H. Cho, S.-J. Na, Implementation of real-time multiple reflection and Fresnel absorption of laser beam in keyhole, J. Phys. D: Appl. Phys. 39 (24) (2006) 5372–5378.
[5] S.S. Lee, T.H. Kim, S.J. Hu, W.W. Cai, J.A. Abell, Joining technologies for automotive lithium-ion battery manufacturing: A review, ASME 2010 international manufacturing science and engineering conference, American Society of Mechanical Engineers, 2010, pp. 541-549.
[6] M.J. Brand, P.A. Schmidt, M.F. Zaeh, A. Jossen, Welding techniques for battery cells and resulting electrical contact resistances, J. Energy Storage 1 (2015) 7–14.
[7] M.J. Brand, P. Berg, E.I. Kolp, T. Bach, P. Schmidt, A. Jossen, Detachable electrical connection of battery cells by press contacts, J. Energy Storage 8 (2016) 69–77.
[8] T. Solchenbach, P. Plapper, W. Cai, Electrical performance of laser braze-welded aluminum–copper interconnects, J. Manuf. Process. 16 (2) (2014) 183–189.
[9] K. Lee, S. Yi, S. Hyun, C. Kim, Review on the Recent Welding Research with Application of CNN-Based Deep Learning Part I: Models and applications, J. Weld. Joining 39 (1) (2021) 10–19.
[10] K. Lee, S. Yi, S. Hyun, C. Kim, Review on the Recent Welding Research with Application of CNN-Based Deep Learning Part II: Model evaluation and visualizations, J. Weld. Joining 39 (1) (2021) 20–26.
[11] S. Lee, S.-J. Na, A study on automatic seam tracking in pulsed laser edge welding by using a vision sensor without an auxiliary light source, J. Manuf. Sys. 21 (4) (2002) 302–315.
[12] S.-K. Lee, S.-J. Na, A Study on weld pool monitoring in pulsed laser edge welding, Proceedings of the KWS Conference, The Korean Welding and Joining Society, 2002, pp. 595-599.
[13] Y. Zhang, D. You, X. Gao, S. Katayama, Online Monitoring of Welding Status Based on a DBN Model During Laser Welding, Eng. 5 (4) (2019) 671–678.
[14] B. Zhang, K.-M. Hong, Y.C. Shin, Deep learning-based porosity monitoring of laser welding process, Manuf. Lett. 23 (2020) 62–66.
[15] Z. Zhang, B. Li, W. Zhang, R. Lu, S. Wada, Y. Zhang, Real-time penetration state monitoring using convolutional neural network for laser welding of tailor rolled blanks, J. Manuf. Sys. 54 (2020) 348–360.
[16] K. Lee, S. Kang, M. Kang, S. Yi, S. Hyun, C. Kim, Modeling of Laser Welds Using Machine Learning Algorithm Part I: Penetration Depth for Laser Overlap Al/Cu Dissimilar Metal Welds, J. Weld. Joining 39 (1) (2021) 27–35.
[17] B.-S. Go, H. You, H.-S. Bang, C. Kim, Penetration Depth Modeling and Process Parameter Maps for Laser Welds Using Machine Learning, J. Weld. Joining 39 (4) (2021) 392–401.
[18] H. You, M. Kang, S. Yi, S. Hyun, C. Kim, Modeling of Laser Welds Using Machine Learning Algorithm Part II: Geometry and Mechanical Behaviors of Laser Overlap Welded High Strength Steel Sheets, J. Weld. Joining 39 (1) (2021) 36–44.
[19] K. Lee, S. Kang, M. Kang, S. Yi, C. Kim, Estimation of Al/Cu laser weld penetration in photodiode signals using deep neural network classification, J. Laser Appl. 33 (4) (2021), 042009.

[20] F. Chollet, Deep Learning with Python, Manning Publications Co., Shelter Island, NY, USA, 2018.
[21] D.P. Kingma, J. Ba, Adam: A method for stochastic optimization, arXiv preprint arXiv:1412.6980 (2014).
[22] C. Knaak, P. Abels, AI-based quality monitoring of auto-body weld joints in real time: Christian Knaak and Peter Abels, of Fraunhofer ILT, explain how imaging and machine learning can be used to identify weld imperfections with high accuracy, Laser Systems Europe 47 (2020) 12–14.
[23] Y. Yang, L. Pan, J. Ma, R. Yang, Y. Zhu, Y. Yang, L. Zhang, A High-Performance Deep Learning Algorithm for the Automated Optical Inspection of Laser Welding, Appl. Sci. 10 (3) (2020) 933.
[24] C. Knaak, J. von Essen, M. Kroger, F. Schulze, P. Abels, A. Gillner, A Spatio-Temporal Ensemble Deep Learning Architecture for Real-Time Defect Detection during Laser Welding on Low Power Embedded Computing Boards, Sensors (Basel) 21 (12) (2021).
[25] C. Knaak, M. Kröger, F. Schulze, P. Abels, A. Gillner, Deep learning and conventional machine learning for image-based in-situ fault detection during laser welding: A comparative study Preprint (2021).
[26] Y. Zhang, D. You, X. Gao, N. Zhang, P.P. Gao, Welding defects detection based on deep learning with multiple optical sensors during disk laser welding of thick plates, J. Manuf. Sys. 51 (2019) 87–94.
[27] W. Cai, P. Jiang, L. Shu, S. Geng, Q. Zhou, Real-time identification of molten pool and keyhole using a deep learning-based semantic segmentation approach in penetration status monitoring, J. Manuf. Process. 76 (2022) 695–707.
[28] J.H.A.J.M.S.O. Wehner Camera-based spatter detection in laser welding with a deep learning approach, FORUM BILDVERARBEITUNG 2020, 2020.
[29] C. Kim, J. Kim, J. Kim, S. Rhee, Estimation of penetration depth by using coaxial image monitoring during laser lap welding, International Congress on Applications of Lasers & Electro-Optics, Laser Institute of America, 2007, p. 1503.
[30] C.-H. Kim, D.-C. Ahn, Coaxial monitoring of keyhole during Yb:YAG laser welding, Opt. Laser Technol. 44 (6) (2012) 1874–1880.
[31] A. Sun, E. Kannatey-Asibu, M. Gartner, Sensor systems for real-time monitoring of laser weld quality, J. Laser Appl. 11 (4) (1999) 153–168.
[32] P. Norman, H. Engström, A.F.H. Kaplan, Theoretical analysis of photodiode monitoring of laser welding defects by imaging combined with modelling, J. Phys. D: Appl. Phys. 41 (19) (2008).
[33] R. Olsson, I. Eriksson, J. Powell, A.V. Langtry, A.F.H. Kaplan, Challenges to the interpretation of the electromagnetic feedback from laser welding, Opt. Lasers Eng. 49 (2) (2011) 188–194.
[34] D.Y. You, X.D. Gao, S. Katayama, Review of laser welding monitoring, Sci. Technol. Weld. Joining 19 (3) (2013) 181–201.
[35] W. Cai, J. Wang, P. Jiang, L. Cao, G. Mi, Q. Zhou, Application of sensing techniques and artificial intelligence-based methods to laser welding real-time monitoring: A critical review of recent literature, J. Manuf. Sys. 57 (2020) 1–18.
[36] M. Kang, I.-H. Jeon, H. Han, C. Kim, Tensile–shear fracture behavior prediction of high-strength steel laser overlap welds, Met. 8 (5) (2018) 365.
[37] T. Bautze, M. Kogel-Hollacher, Keyhole depth is just a distance: The IDM sensor improves laser welding processes, Laser Tech. J. 11 (4) (2014) 39–43.
[38] M. Boley, R. Weber, T. Graf, Online detection of pore formation during laser deep-penetration welding, Proceeding of lasers in manufacturing congress (LIM), 2015.
[39] M. Sokolov, P. Franciosa, T. Sun, D. Ceglarek, V. Dimatteo, A. Ascari, A. Fortunato, F. Nagel, Applying optical coherence tomography for weld depth monitoring in remote laser welding of automotive battery tab connectors, J. Laser Appl. 33 (1) (2021), 012028.
[40] N.D. Dupriez, C. Truckenbrodt, OCT for Efficient High Quality Laser Welding: High-speed, high-resolution online seam tracking, monitoring and quality control, Laser Tech. J. 13 (3) (2016) 37–41.
[41] M. Boley, F. Fetzer, R. Weber, T. Graf, Statistical evaluation method to determine the laser welding depth by optical coherence tomography, Opt. Lasers Eng. 119 (2019) 56–64.
[42] C. Stadter, M. Schmoeller, M. Zeitler, V. Tueretkan, U. Munzert, M.F. Zaeh, Process control and quality assurance in remote laser beam welding by optical coherence tomography, J. Laser Appl. 31 (2) (2019), 022408.
[43] C. Stadter, M. Schmoeller, L. von Rhein, M.F. Zaeh, Real-time prediction of quality characteristics in laser beam welding using optical coherence tomography and machine learning, J. Laser Appl. 32 (2) (2020), 022046.